Development of Versatile Multi-Link MIMO Channel Sounding Sensor Network Using Software-Defined Radios

Minseok KIM†, Togo IKEGAMI†, and Masamune SATO†

† The Graduate School of Science and Technology, Niigata University, Niigata 950-2181, Japan

E-mail: †mskim@eng.niigata-u.ac.jp

Abstract In this study, we develop a versatile multi-link MIMO channel sounding sensor network based on software-defined radios (SDRs). Each radio has a center frequency of 4.85 GHz, a bandwidth of 100 MHz, and a delay time resolution of 10 ns. It can accommodate a large number of antennas using a switched antenna scheme; further, by associating multiple software radios, it can configure a multi-link MIMO measurement and obtain the synchronized channel responses in a short time. It is suitable for various purposes of channel measurements, such as distributed massive MIMO, cell-free MIMO, localization, and sensing. This paper presents the design and implementation of the developed system and verifies the synchronized operation through laboratory tests. Then, the usability is demonstrated through an example measurement for indoor device-free localization (DFL).

Key words multi-link channel sounding, MIMO channels, distributed MIMO, massive MIMO, cell-free MIMO

1. Introduction

Recently, distributed antenna networks, such as distributed massive MIMO [1], cell-free MIMO [2], localization, and sensing, that leverage a large number of antennas spatially distributed rather than being collocated in a single array, have emerged. Channel measurement and modeling are essential components of designing and evaluating such a new wireless system. Thus, channel-sounding techniques to efficiently obtain the multi-link radio channels among the distributed massive number of antennas [3] are required.

To cope with the challenge mentioned above, this paper developed a versatile multi-link MIMO channel sounding sensor network based on a switched antenna channel sounding scheme based on software-defined radios (SDRs) [4]. This paper presents the design and implementation of the developed system and verifies the synchronized operation through laboratory tests. Then, the usability is demonstrated through an example measurement for indoor device-free localization (DFL) [5–7].

2. Switched Antenna MIMO Channel Sounder

2.1 Software Defined Radio

SDR has high flexibility by implementing the functions of wireless communication systems in software, allowing for the realization of various wireless transmission techniques without the need for hardware changes. In particular, an open-source development environment, universal software radio peripheral (USRP) (by Ettus Research, USA), is popular for easy and cost-effective prototyping, and it can realize a wide variety of wireless communication techniques using open-source software platform GNU Radio [4]. The USRP-based prototyping utilizes not only GNU Radio but also software platforms such as LabVIEW and MATLAB/Simulink. Additionally, a driver and application programming interface (API) called USRP hardware driver (UHD) is provided, which allows for more advanced control using programming languages such as C/C++ and Python.

In this study, we adopt the USRP X310, which consists of a motherboard and two RF daughterboards (UBX 160) with a frequency range from 10 MHz to 6 GHz and a maximum passband bandwidth of 160 MHz. For the interface between the USRP and host PC, 10 Gigabit Ethernet is adopted, allowing for data transfer at up to 200 MS/s (max. passband bandwidth: 200 MHz). However, the maximum bandwidth in this configuration is determined by the low pass filter (LPF) of the daughterboards.

The signal flows for transmitting and receiving are as follows. First, on the transmitting side, the complex baseband signal sent from the host PC undergoes interpolation processing by the digital upconverter (DUC), converting it into a complex signal at an intermediate frequency (IF) near DC. Then, the IF digital signal is converted into an analog signal via a high-speed DAC and input into the RF upconverter circuit of the daughterboard. On the receiving side, the received signal is downconverted to a complex signal at an IF near DC and sampled by a high-speed ADC. After that, it is converted into a complex baseband signal by the digital downconverter (DDC) inside the FPGA and finally transferred to the host PC.

2.2 Switched Antenna Multiplexing Scheme

An RF switch connected to the daughterboard's antenna port is used to switch the antennas to realize a switched antenna scheme. The RF switch used is the SR-J030-8S (Universal Microwave Components Corp.), of which detailed specifications are shown in Table 1. The USRP X310 features 15-pin general-purpose input/output (GPIO) ports which are directly controlled by the FPGA on the motherboard. The UHD API provides functions to operate the GPIO ports, and those are used to control the RF switch in the developed system. Fig. 1 shows the control sequence diagram for antenna switching. The transmitter (Tx) transmits twice the number of sounding signals for the number of receiving antenna elements, then switches the Tx antenna, and the re-

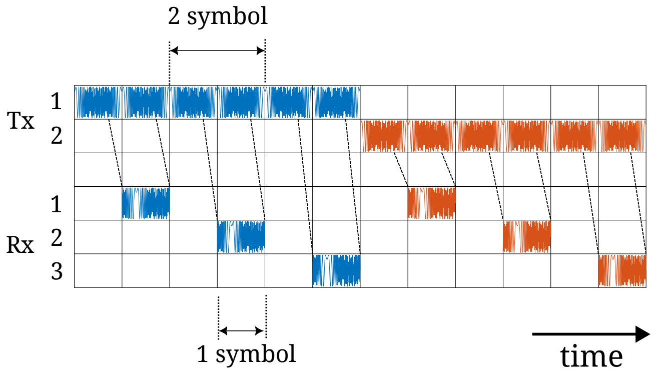

Fig. 1 Sequence diagram of antenna switching process (for 2×3 MIMO)

Table 1 Specifications of the RF switch.

Item	Specification
Frequency range	0.5–12.4 GHz
Insertion loss	3.0 dB Max
Isolation	0.5–6 GHz: 60 dB Min 6–12.4 GHz: 50 dB Min
VSWR (on state)	1.8:1 Max
Rise/Fall time[*a]	40 ns Max
On/Off time[*b]	90 ns Max

[*a] 10–90%RF, 90–10%RF
[*b] 50%TTL–90%RF, 50%TTL–10%RF

Table 2 Measurement system specifications.

Item	Specification
Carrier frequency	4.85001 GHz
Sampling frequency	200 MHz
Signal bandwidth	100 MHz
Sounding signal	Multitone signal [3]
No. subcarriers	256
Subcarrier interval	781.25 kHz
Symbol length	1.28 us
Delay resolution	10 ns
FFT points	256
Transmit power	15 dBm (typ.)
Measurement time	164 us (8×8 MIMO)

ceiver (Rx) switches antennas over a period twice the length of the sounding signal. This allows the capture of the sounding signal even with some time delay caused by propagation and RF switching.

The detailed measurement system specifications are shown in Table 2. Due to the roll-off characteristics of the DDC, which distorts both ends of the transfer function, the middle 128 points out of the 256 points of the obtained transfer function, excluding 64 points from both ends, are used. As a result, the passband signal bandwidth becomes 100 MHz although the sampling frequency is 200 MHz.

2.3 Evalution of Phase Stability

Accurate measurement of phase information is crucial in MIMO channel sounding, and the coherence of received signals between elements plays a significant role in array signal processing. A switched antenna MIMO channel sounder repeatedly transmits the same sounding signal and sequentially switches the Tx and Rx antennas to measure all channels. Therefore, phase drift during the measurement can significantly degrade the accuracy of array signal processing.

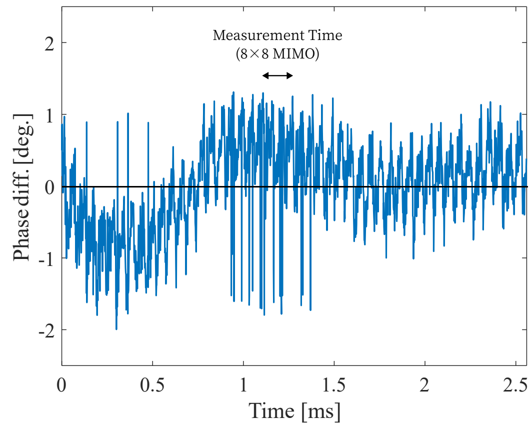

(a) Phase stability of the local oscillator.

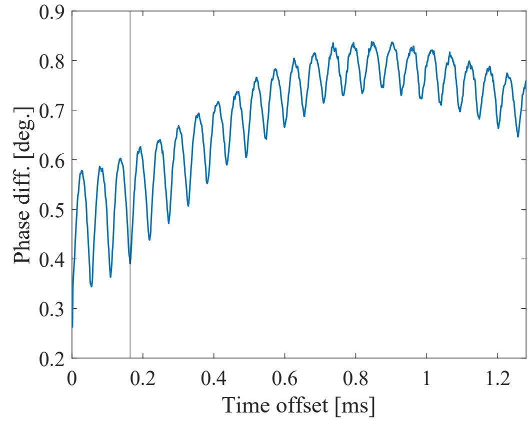

(b) Average absolute phase difference at each time offset.

Fig. 2 Phase stability evaluation.

Hence, we evaluated the phase stability of the local oscillator.

The evaluation was conducted by directly connecting the Tx antenna port and Rx antenna port through an attenuator, transmitting a sounding signal, and measuring the phase of the received signal. The measurement results are shown in Fig. 2(a). Here, phase variation was calculated by taking the average phase across all subcarriers and measuring the phase difference at each time sample with respect to the first sample. The results showed that the maximum phase difference was approximately 3°, with a standard deviation of 0.62°. Furthermore, the average absolute phase difference with respect to time offset is shown in Fig. 2(b). The vertical solid line in the figure indicates the time required for 8×8 MIMO measurement (approximately 164 us). The average absolute phase difference for the measurement duration is found to be approximately 0.4°–0.6°. It is considered that the impact of the switched antenna scheme is minimal, and the results are sufficiently acceptable for array signal processing.

3. Multi-Link MIMO Channel Sounding Sensor Network

In this section, we describe the multi-link MIMO channel sounding system developed to efficiently obtain the radio channels among the distributed massive number of antennas. Each node has an 8-element switched antenna array for Tx/Rx (half-duplex) and is designed to measure the impulse responses of the 8×8 MIMO channels between each pair of nodes. The system is designed to be scalable, and in this

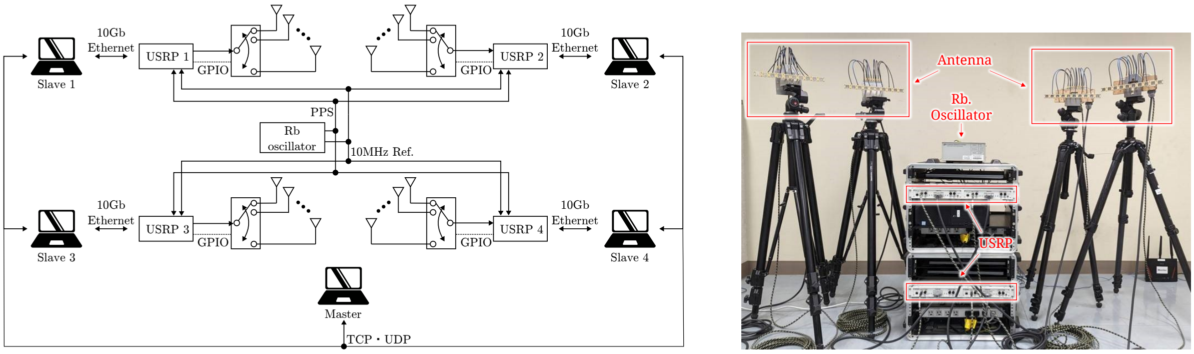

(a) Block diagram. (b) Photograph.

Fig. 3 6 link MIMO channel measurement configuration with 4 nodes.

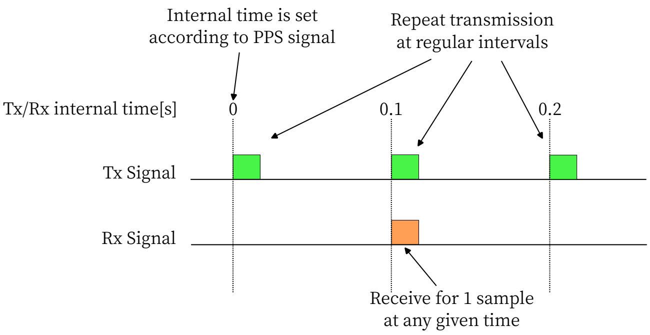

Fig. 4 Timing synchronization for transmission and reception.

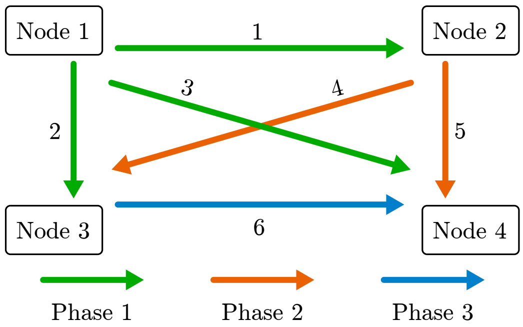

Fig. 5 6 link measurement procedure with 4 nodes.

study, it is configured as a 6 link system with 4 nodes.

3.1 Multi-Link Channel Measurement Scheme

Each node has an 8-element switched antenna array for Tx/Rx, and the propagation path between each pair of nodes is defined as a link. When N denotes the number of nodes, there exist $\binom{N}{2}$ links. In this study, we designed a six-link channel measurement system with four nodes. Fig. 3 shows an overview of the measurement system. Each node is equipped with one USRP, and a slave PC controls each USRP. Additionally, there is a master PC that sends transmission and reception commands to the slave PCs. The communication is carried out through TCP, and the data received by each slave PC is sent to the master PC using UDP.

3.2 Timing Synchronization

To achieve propagation channel measurements with physically separated multiple radio transceivers, carrier frequency, and transmission/reception timing must be synchronized among them. USRPs have 10 MHz REF and pulse-per-second (PPS) ports, which function as interfaces for synchronizing multiple devices. In this study, the REF and PPS signals generated by a rubidium oscillator are commonly input to each node's USRP, achieving frequency and timing synchronization between the nodes. The UHD API provides a function to set the USRP device time synchronized with the PPS. By using this function to set the device time to 0 when communication between the USRP device and the host PC is established, the USRP device time is synchronized with the PPS signal. This synchronizes the internal time (elapsed time from PPS) between the nodes. Fig. 4 shows an image of the synchronized transmission and reception timing. According to this figure, the Tx transmits the sounding signal every 100 ms. The receiver receives the signal of an arbitrary transmission cycle. The timing of transmission and reception can be specified by setting the device time to start transmission and reception using the function provided by the UHD API.

3.3 Multilink Measurement Procedure

By the method described above, it is possible to measure the impulse responses of the MIMO channels for each Tx-Rx node pair. This is extended to realize multi-link measurement by appropriately switching the transmission or reception mode of each node. Fig. 5 shows the Tx-Rx pairs for each link measurement. In this scheme, the measurement of all links is divided into three phases. In the first phase, `Node 1` is set as the Tx node, and measurements for `Links 1` to `3` are conducted. In the second phase, `Node 2` is set as the Tx node, and measurements for `Links 4` to `5` are conducted. Finally, in the third phase, `Node 3` is set as the Tx node, and the measurement for `Link 6` is conducted.

In each phase, communication is carried out between the master PC and slave PCs as shown in Fig. 6. To ensure that transmission has started, the command to start reception on the Rx slave PC is given after receiving a transmission start notification from the Tx slave PC. The Tx node, upon receiving the transmission start command, transmits continuously at intervals of 100 ms. On the other hand, the Rx node, upon receiving the reception start command, receives the necessary samples in accordance with the transmission timing. If there are multiple Rx nodes, a broadcast is made to each slave PC on the Rx side to start reception simultaneously. The received data is transferred to the master PC via UDP by each slave PC. On the master PC side, the received data is checked, and the transmission for the next phase is started. Furthermore, to speed up the process, it is also possible to save the received data on each slave PC and skip the data transfer to the master PC, moving directly to the next

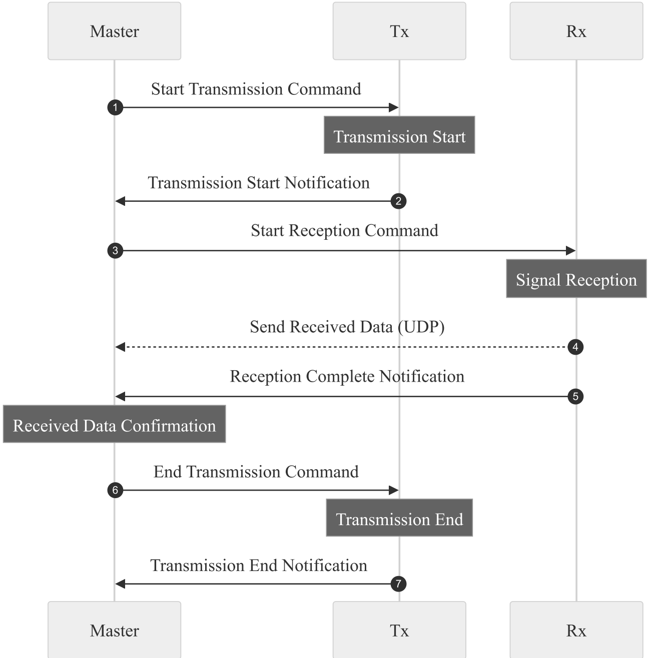

Fig. 6 Communication flow diagram.

Table 3 Node coordinates, (x, y) [m], in two deployment configuration.

Anchor Node	Config. 1	Config. 2
1	$(1.6, 0.0)$	$(4.5, 0.0)$
2	$(0.2, 4.75)$	$(0.0, 2.0)$
3	$(4.0, 5.68)$	$(1.5, 5.68)$
4	$(7.04, 2.0)$	$(7.04, 4.75)$

phase.

4. Evaluation of Multi-Link MIMO Measurement System

In this section, we evaluate the operation of the multi-link MIMO channel sounding network developed in the previous section.

4.1 Measurement Environment and Specifications

In this system, a 6 link 8×8 MIMO channel measurement was conducted with 4 nodes. Each node was equipped with an equally spaced linear array antenna with an element spacing of half a wavelength. Fig. 7 shows the measurement environment. Propagation channel measurements were conducted with two types of antenna arrangements, as shown in Fig. 7(b). The positions of the anchor nodes for each antenna deployment are shown in Table 3. Since the anchor nodes' positions differ, two datasets were combined to extend to 12 link measurements with 8 nodes. Fig. 8 shows the propagation paths obtained by RT simulation for 12 links.

4.2 MIMO CTFs and CIRs

Fig. 9 shows an excerpt of the channel measurement results for the link between `Node 1` for Tx and `Node 3` for Rx, under Config 1. The straight-line distance of this link is 6.17 m, hence the theoretical value of the delay time is 20.6 ns. Furthermore, the free space propagation loss is 62.0 dB, and since the gain of the Tx and Rx antennas is 4 dBi, the theoretical value of the propagation loss is 54.0 dB. As seen in Fig. 9(b), there is a peak around the delay time of 20

(a) Measurement scene.

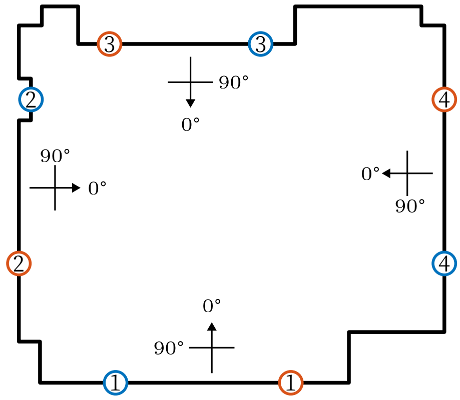

(b) Antenna deployment configurations (Blue: Config. 1, Orange: Config. 2).

Fig. 7 Channel measurement environment.

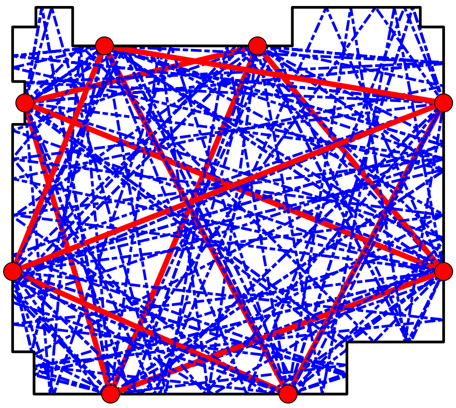

Fig. 8 Propagation paths obtained by RT simulation

ns, and the received power is confirmed to be approximately $-50 \sim -60$ dB. Given that the delay time resolution of the developed system is 10 ns, it can be seen that the results obtained are reasonable in comparison to the theoretical values.

4.3 DFL Evaluation

4.3.1 Multipath-RTI Technique

In the radio tomographic imaging (RTI) method [5], the received signal strength (RSS) values $\mathbf{y} \in \mathbb{R}^N$ for each propagation path are represented as the linear sum of voxel values along the propagation path as

$$\mathbf{y} = \mathbf{W}\mathbf{x} + \mathbf{n}, \tag{1}$$

where $\mathbf{x} \in \mathbb{R}^M$ represents the voxel values in the target localization area, and $\mathbf{n} \in \mathbb{R}^N$ is zero mean white Gaussian noise process. The change in RSS due to power attenuation caused by obstruction at time t is,

$$\Delta\mathbf{y}(t) = \mathbf{W}\Delta\mathbf{x}(t) + \Delta\mathbf{n}(t) \tag{2}$$

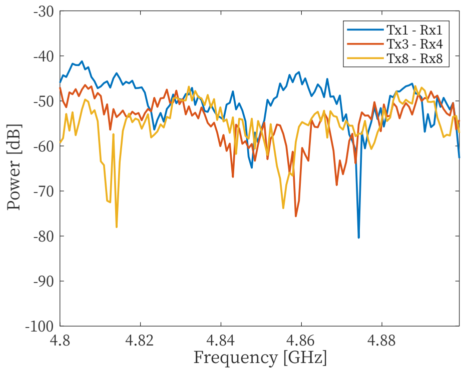

(a) Transfer function.

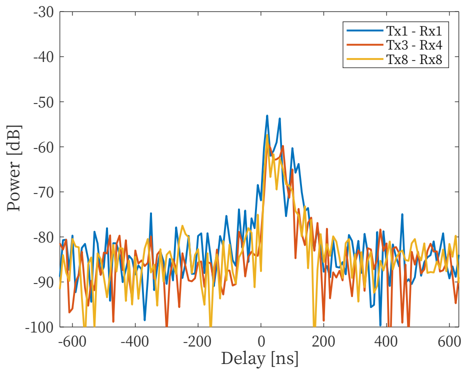

(b) Impulse response.

Fig. 9 Example of MIMO channel measurement results (Legend: Element number of Tx and Rx antennas)

where $\Delta\mathbf{y}(t) = \mathbf{y}(t) - \mathbf{y}_0$, $\Delta\mathbf{x}(t) = \mathbf{x}(t) - \mathbf{x}_0$, and $\Delta\mathbf{n}(t) = \mathbf{n}(t) - \mathbf{n}_0$. Moreover, $\mathbf{y}_0$, $\mathbf{x}_0$, and $\mathbf{n}_0$ are the values of the baseline measurement. $\mathbf{W} \in \mathbb{R}^{N\times M}$ is a matrix for weighting the voxels along the line-of-sight (LoS) path and is defined by

$$[\mathbf{W}]_{ij} = w_{ij} = \begin{cases} 1/\sqrt{d_l}, & d_{l,s}^m + d_{l,d}^m < d_l + \gamma \\ 0, & \text{elsewhere} \end{cases} \tag{3}$$

Here, d_l is the distance between nodes in the lth link, $d_{l,s}^m$ and $d_{l,d}^m$ are the distances from the mth voxel to the Tx and Rx nodes, respectively. Furthermore, γ is a parameter that affects the width of weighting.

In the multipath RTI method [6, 7], in addition to the direct wave, reflected waves up to two reflections are utilized. Specifically, it is assumed that the reflected waves are generated by virtual sensor nodes outside the localization target area, and conditions considering this are added to the weighting matrix as

$$[\mathbf{W}]_{ij} = w_{ij} = \begin{cases} 1/\sqrt{d_l}, & d_{l,s}^m + d_{l,r}^m < d_{l,1} + \gamma \\ 1/\sqrt{d_l}, & d_{l,r}^m + d_{l,d}^m < d_{l,2} + \gamma \\ 0, & \text{elsewhere} \end{cases} \tag{4}$$

Here, d_l is the path length of the lth path, $d_{l,s}^m$, $d_{l,d}^m$, and $d_{l,d}^m$ are the distances from the mth voxel to the transmitting node, reflection point, and receiving node, respectively.

To realize multipath RTI, it is necessary to know the changes in RSS for each propagation path. In this study, we use array antennas at each anchor node to extract the RSS of individual propagation paths through MIMO beamforming. Specifically, the propagation paths between each link

Table 4 Coordinates of positioning target

Pos.	Target's coordinates (x, y) [m]
A	$(3.52, 3.15)$
B	$(3.00, 1.40)$
C	$(1.40, 4.50)$
D	$(5.50, 3.15)$
E	$(5.50, 5.00)$

Table 5 RTI parameters

Parameter	Value
RTI voxel size	0.05 m
RTI ellipse param., γ	0.05 m
Regularization param., λ	by 5-fold cross-validation
Regularization param., α	0.25
DBSCAN ϵ	0.5 m
DBSCAN N_{minPts}	3

are pre-estimated using ray-tracing simulations based on the simple 3D model of the measurement environment. Then, based on the simulation results, the vector of RSS changes for each link can be obtained through MIMO beamforming for the measured MIMO channel matrix $\boldsymbol{h}$ as

$$\begin{aligned} \Delta\mathrm{y}\left(\phi_{\mathrm{Tx}}, \phi_{\mathrm{Rx}}, \tau\right) = &\left|\boldsymbol{a}^H\left(\phi_{\mathrm{Tx}}, \phi_{\mathrm{Rx}}, \tau\right)\boldsymbol{h}\right|^2 \\ &- \left|\boldsymbol{a}^H\left(\phi_{\mathrm{Tx}}, \phi_{\mathrm{Rx}}, \tau\right)\boldsymbol{h}_0\right|^2, \end{aligned} \tag{5}$$

Here, $\boldsymbol{h}_0$ is the MIMO channel matrix measured when there is no target in the positioning area. Furthermore, $\boldsymbol{a}\left(\phi_{\mathrm{Tx}}, \phi_{\mathrm{Rx}}, \tau\right)$ is the steering vector for the angle of departure (AoD), angle of arrival (AoA), and delay time (DToA). Considering a MIMO configuration using linear array antennas with K elements at half-wavelength intervals for both the transmitter and receiver, when the AoD, AoA, and delay time τ arrive in the broadside direction as ϕ_{Tx}, ϕ_{Rx}, respectively, the amplitude of the received signal is denoted as $\boldsymbol{\Gamma}$, and the MIMO channel matrix for each link is represented as

$$\boldsymbol{h} = \boldsymbol{A}(\boldsymbol{\Omega})\boldsymbol{\Gamma} \in \mathbb{C}^{K^2N\times 1}, \tag{6}$$

$$\boldsymbol{A}(\boldsymbol{\Omega}) = \left[\boldsymbol{a}\left(\Omega_1\right), \ldots, \boldsymbol{a}\left(\Omega_L\right)\right] \in \mathbb{C}^{K^2N\times L}, \tag{7}$$

$$\boldsymbol{\Gamma} = \left[\Gamma_1, \ldots, \Gamma_L\right] \in \mathbb{C}^{L\times 1}, \tag{8}$$

$$\boldsymbol{\Omega} = \left[\Omega_1, \ldots, \Omega_L\right] \in \mathbb{C}^{L\times 1}, \tag{9}$$

$$\boldsymbol{\Omega}_l = \left[\phi_{\mathrm{Tx},l}, \phi_{\mathrm{Rx},l}, \tau_l\right], \tag{10}$$

$$\boldsymbol{a}\left(\boldsymbol{\Omega}_l\right) = \boldsymbol{a}_{\mathrm{T}}\left(\phi_{\mathrm{Tx},l}\right) \otimes \boldsymbol{a}_{\mathrm{R}}\left(\phi_{\mathrm{Rx},l}\right) \otimes \boldsymbol{a}_\tau\left(\tau_l\right), \tag{11}$$

where N and L represent the number of delay time bins and the number of propagation paths, respectively. Moreover, $\otimes$ denotes the Kronecker product operator. The steering vectors for transmission, reception, and delay time are represented as

$$\begin{aligned} \boldsymbol{a}_{\mathrm{R}}\left(\phi_{\mathrm{Rx}}\right) = &\left[1, \exp\left(-\mathrm{j}\pi\sin\phi_{\mathrm{Rx}}\right),\right. \\ &\left.\cdots, \exp\left(-\mathrm{j}\pi(K-1)\sin\phi_{\mathrm{Rx}}\right)\right]^T, \end{aligned} \tag{12}$$

$$\begin{aligned} \boldsymbol{a}_{\mathrm{T}}\left(\phi_{\mathrm{Tx}}\right) = &\left[1, \exp\left(-\mathrm{j}\pi\sin\phi_{\mathrm{Tx}}\right),\right. \\ &\left.\cdots, \exp\left(-\mathrm{j}\pi(K-1)\sin\phi_{\mathrm{Tx}}\right)\right]^T, \end{aligned} \tag{13}$$

$$\boldsymbol{a}_\tau(\tau) = \left[a_\tau\left(\tau_0 - \tau\right), \ldots, a_\tau\left(\tau_{N-1} - \tau\right)\right]^T, \tag{14}$$

$$a_\tau(\tau) = \frac{1}{N}\exp\left(-\mathrm{j}\pi\Delta_f\tau\right)\frac{\sin\pi N\Delta_f\tau}{\sin\pi\Delta_f\tau}, \tag{15}$$

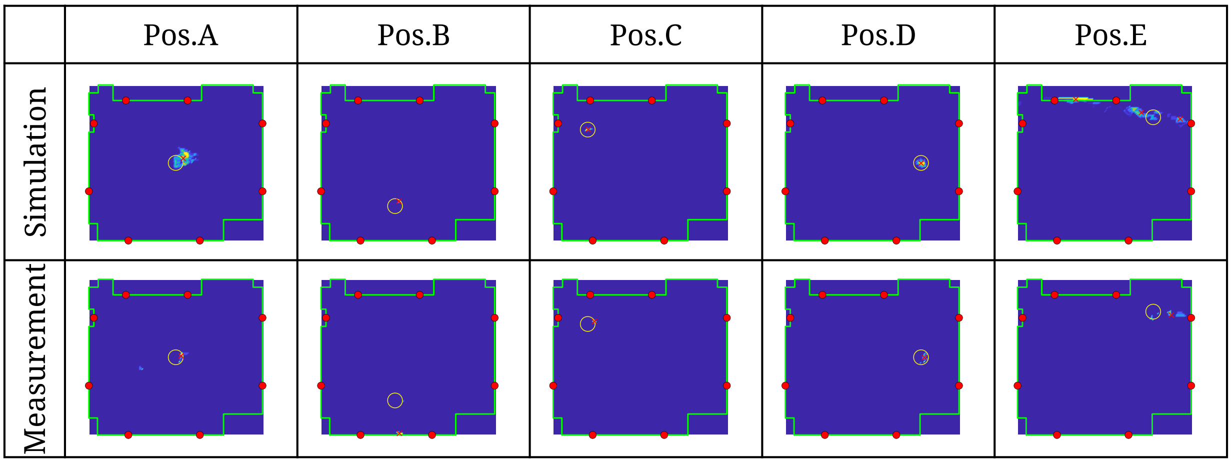

Fig. 10 Generated RTI images and position estimation results

where Δ_f is the frequency sampling interval.

4.3.2 Evaluation Results

We present the results of verifying the effectiveness of the proposed positioning method based on the measurement results obtained by using the developed system. Table 4 shows the positioning target's locations. A radio wave absorber with a radius of 0.3 m was used as the positioning target. Channel measurements were conducted both in the absence of the positioning target (baseline measurement) and with the positioning target in each configuration, and post-processing was performed to generate RTI images and estimate positions.

Fig. 10 shows the RTI images created for the target placed as shown in Table 4 in the measurement environment, where the anchor node deployment was described in section 4. For comparison, RTI images generated by simulation are also shown. Here, the various parameters used for generating the RTI images and position estimation are listed in Table 5. In the figure, the yellow circles represent the actual positions of the positioning targets, and the red crosses represent the results of the position estimation.

From the measurement results, it can be seen that the estimated positions are generally in the vicinity of the actual target positions. For `Pos E`, there are artifact images in the results generated by simulation as well, making theoretical estimation difficult; therefore, the estimation accuracy is lower compared to other positions in the measurement results. On the other hand, for `Pos B`, the simulation was able to estimate the position within the radius of the positioning target, but the measurement results estimated it at a distance position. It is seen that, for `Pos B`, the direct wave path is not obstructed, and the influence of the RSS estimation of the reflected waves is larger compared to other positions. Additionally, the difference between the actual propagation path and that generated by RT simulation could lead to a degradation in estimation accuracy. That is, there might be paths that exist in the RT simulation but not in reality, or vice versa. To solve this, it is necessary to compare the measurement results with the RT simulation results and remove the paths that do not actually exist. Furthermore, by extracting MPCs from the measurement values and associating them with the results of the RT simulation, it is expected that more accurate RTI images can be generated.

5. Conclusion

In this study, we developed a system capable of multi-link MIMO channel measurement in a short period, aimed at various scenarios of a distributed massive number of antennas, and verified its effectiveness. The system utilizes the USRP X310 software radio to implement antenna switching MIMO techniques and enables simultaneous measurement of multiple links by associating multiple USRPs. We conducted multi-link MIMO channel measurements in a typical room to verify the system.

Acknowledgement

This work was supported by JAEA Nuclear Energy S&T and Human Resource Development Project Grant Number JPJA22P22683407.

References

[1] D. Löschenbrand, M. Hofer, L. Bernado, G. Humer, B. Schrenk, S. Zelenbaba, and T. Zemen, "Distributed Massive MIMO Channel Measurements in Urban Vehicular Scenario," in *2019 13th European Conference on Antennas and Propagation (EuCAP)*, Mar. 2019.

[2] H. Q. Ngo, A. Ashikhmin, H. Yang, E. G. Larsson, and T. L. Marzetta, "Cell-Free Massive MIMO Versus Small Cells," *IEEE Trans. Wireless Commun.*, vol. 16, no. 3, pp. 18341850, Mar. 2017.

[3] M. Kim, J. Takada, and Y. Konishi, "Novel Scalable MIMO Channel Sounding Technique and Measurement Accuracy Evaluation With Transceiver Impairments," *IEEE Trans. Instrum. Meas.*, vol. 61, no. 12, pp. 3185–3197, Feb. 2012.

[4] Ettus Research, USRP X310 High Performance Software Defined Radio. [Online]. Available: https://www.ettus.com/all-products/x310-kit/

[5] J. Wilson and N. Patwari, "Radio Tomographic Imaging with Wireless Networks," *IEEE Trans. Mobile Comput.*, vol. 9, no. 5, pp. 621-632, May 2010.

[6] Togo Ikegami, Minseok Kim, Yuto Miyake, Hibiki Tsukada, "Multipath RTI: Millimeter-Wave Radio Based Device-Free Localization," *IEEE Access*, vol. 12, pp. 42042–42054, 202

[7] M. Kim, Y. Miyake, T. Ikegami, H. Tsukada, and K. Kumakura, "Device-Free Localization Using Millimeter-Wave Double-Directional Channel Sounding Measurements," in 2022 16th European Conference on Antennas and Propagation (EuCAP), Mar. 2022, pp. 1-4.